Rapid Communication

Pyrochlore-based high-entropy ceramics for capacitive energy storage

Yiying CHEN, Junlei QI, Minhao ZHANG, Zixi LUO, Yuan-Hua LIN[*]

State Key Laboratory of New Ceramics and Fine Processing, School of Materials Science and Engineering, Tsinghua University, Beijing 100084, China

Abstract: High-performance dielectrics are widely used in high-power systems, electric vehicles, and aerospace, as key materials for capacitor devices. Such application scenarios under these extreme conditions require ultra-high stability and reliability of the dielectrics. Herein, a novel pyrochlore component with high-entropy design of $Bi_{1.5}Zn_{0.75}Mg_{0.25}Nb_{0.75}Ta_{0.75}O_7$ (BZMNT) bulk endows an excellent energy storage performance of $W_{rec} \approx 2.72$ J/cm^3 together with an ultra-high energy efficiency of 91% at a significant enhanced electric field E_b of 650 kV/cm. Meanwhile, the temperature coefficient (TCC) of BZMNT (~ -220 ppm/℃) is also found to be greatly improved compared with that of the pure $Bi_{1.5}ZnNb_{1.5}O_7$ (BZN) (~ -300 ppm/℃), demonstrating its potential application in temperature-reliable conditions. The high-entropy design results in lattice distortion that contributes to the polarization, while the retardation effect results in a reduction of grain size to submicron scale which enhances the E_b. The high-entropy design provides a new strategy for improving the high energy storage performance of ceramic materials.

Keywords: high entropy; bismuth-based pyrochlore; high-temperature stability; energy storage

1 Introduction

The rapid development in electronic and electrical power systems has put forward more demands on electrostatic capacitors including ultrafast charging/discharging speed and long cycling life [1–4]. Although some progress has been made, further improvements in energy density are still required to achieve the miniaturization of capacitors. [5–7]. Recently, the strategy utilizing configurational entropy to modulate material with tailor-made properties with wide application has received much attention [8–10]. The high-entropy oxide (HEO)

concept is originated from the alloy system [11–13], and further widened by the successful fabrication of the binary oxide $(Mg_{0.2}Zn_{0.2}Cu_{0.2}Co_{0.2}Ni_{0.2})O$ in 2015 by Rost *et al.* [14]. Since then, the high-entropy oxides with different crystal structure including rock salt [15], fluorite [16], pyrochlore [17], perovskite [18], and spinel [19] have been paid attention. For example, fluorite-type $(Ce_{0.2}Zr_{0.2}Hf_{0.2}Sn_{0.2}Ti_{0.2})O_2$ ceramic was fabricated by Chen *et al.* [16]; spinel-type $(Co,Cr,Fe,Mn,Ni)_3O_4$ oxide was first successfully synthesized by Stygar *et al.* and the corresponding phase/microstructure was further characterized [19]. Likewise, the perovskite-type $(Bi_{0.2}Na_{0.2}K_{0.2}La_{0.2}Sr_{0.2})TiO_3$ ceramic with satisfactory grain size possessing an energy storage density of 0.959 J/cm^3 was reported by Yang and Zheng [20]. The effects of the entropy design can be summarized as

---

* Corresponding author.

E-mail: linyh@tsinghua.edu.cn

follows [21]: (1) stabilization of the solid-solution formation through promoting dissolution limit among various elements; (2) retardation of the grain growth and reduced grain size; (3) strengthened and hardened structure which contributes to the lattice distortion brought by the mismatch of ionic radii; and (4) unpredictable properties brought by mixing various component elements which is called cocktail effect.

Pyrochlore structure with $A_2B_2O_7$ ($A_2B_2O_6O'$) formula contains a larger-sized cation A which usually has a preferred site coordination number of 8, and a smaller cation B with coordination number of 6 which locates in its octahedral site point [22]. Owing to the compositional and structural flexibility, homovalent or heterovalent ions of different sizes can be doped into the structure. Bismuth-based pyrochlore, typically $Bi_{1.5}ZnNb_{1.5}O_7$ (also can be written as $(Bi_{1.5}Zn_{0.5})(Zn_{0.5}Nb_{1.5})O_7$ in the form of $A_2B_2O_7$) with moderate dielectric constants ($\varepsilon_r \approx$ 180), low dielectric loss ($\sim 10^{-4}$), and low temperature coefficient of resonance frequency (τ_f), has been comprehensively studied in the field of high-frequency and microwave dielectrics [23]. Moreover, the relative low sintering temperature makes it more compatible with Ag electrodes when taking its application in multilayer ceramic capcitors (MLCC) into account [24]. Over the past few decades, investigations related to BZN concentrated on their fabrication methods, phase structure, tenability, and dielectric properties; however, few efforts were made in exploring their energy storage performance [25–28].

Herein, by utilizing high-entropy concept, we have successfully synthesized the high-entropy pyrochlore-based bulk ceramics. It was the first time to study their performance in the capacitive energy storage field systematically. The effects of configurational entropy design on structure, microstructure, dielectric properties, and ferroelectric energy storage performance were studied.

2   Experimental

The $Bi_{1.5}ZnNb_{1.5}O_7$ (BZN), $Bi_{1.5}Zn_{0.75}Mg_{0.25}Nb_{1.5}O_7$ (BZMN), $Bi_{1.5}ZnNb_{0.75}Ta_{0.75}O_7$ (BZNT), and $Bi_{1.5}Zn_{0.75}Mg_{0.25}Nb_{0.75}Ta_{0.75}O_7$ (BZMNT) ceramics were fabricated by conventional solid-state method. Reagent grade oxide powders of Bi_2O_3 (3% excess), ZnO, Nb_2O_5, MgO, Ta_2O_5 were used as raw reactants with proper mass ratio. After the ball-milling process, the samples were dried and calcined at 800–850 ℃ for 3 h. Then, the calcined powders were ball milled again and pressed into disks with PVA binder (φ = 12 mm). Finally, the pellets were sintered at temperature range of 1000–1150 ℃.

The crystal structure and lattice parameters of the four samples were characterized by an X-ray diffractometer (XRD, PANalytical). The microstructure images were obtained by scanning electron microscopy (SEM, Zeiss Gemini). Before the SEM observation, the samples were thermally etched at 50 ℃ lower than each sintering temperature for 20 min. For the dielectric measurements, the polished pellets were pasted with high-temperature silver (φ = 4 mm) on both sides, and tested by a temperature chamber and LCR meter system (Novocontrol, Concept 80). The electrical characterization (*P–E* loop and breakdown strength) was measured by a ferroelectric tester (PK-CPE1701PolyK Tech), the disk samples were polished down to a thickness range of 80–100 μm, and the sputtered Au electrodes were used as electrodes.

3   Results and discussion

The BZN, BZMN, BZNT, and BZMNT were fabricated via solid-phase method. The configurational entropy can be described as [29]:

$$S = -R\left[\left(\sum_{i=1}^{N} x_i \ln x_i\right)_{\text{cation-site}} + \left(\sum_{j=1}^{M} x_j \ln x_j\right)_{\text{anion-site}}\right] \quad (1)$$

where R is the gas constant, and the mole fractions of elements present in the cationic and anionic sites can be represented as x_i and x_j, respectively.

The entropy of BZN, BZMN, BZNT, and BZMNT are calculated to be 1.12, 1.30, 1.64, and 1.81, respectively only when considering 25% Mg^{2+} ions substituting for Zn^{2+} in single A- or B-site. In this case, the firing temperatures of the samples with Mg^{2+} and/or Ta^{5+} dopants exhibit about 50–100 ℃ higher than bare BZN ceramic. All the samples show relative high density over 98%.

The XRD patterns of bismuth niobium zinc oxide pyrochlore ceramic BZN and its high-entropy derivates are displayed in Fig. 1. Four samples all exhibit pure $A_2B_2O_7$ phase (PDF No. 52-1770, *Fd3m*) without detectable impurity. The Ta^{5+} and Nb^{5+} show the same ionic radii of 0.64 Å in the coordination number of 6 in B-site, while the ionic radius of Mg^{2+} with 8 coordination (0.89 Å) is smaller than that of the Zn^{2+} (0.90 Å), leading to the shrinkage of lattice volume as well as the shift of diffraction peaks to a higher degree. The
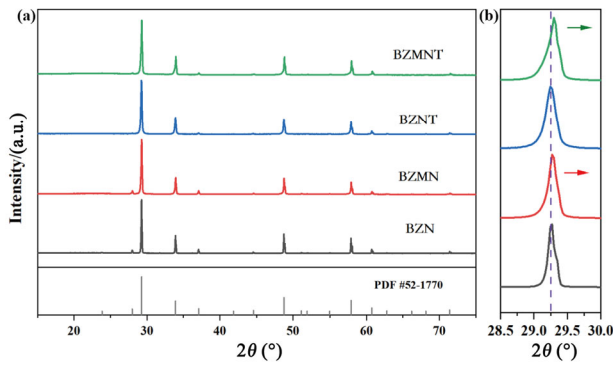
Fig. 1 XRD patterns of BZN, BZMN, BZNT, and BZMNT (a) and their enlarged reflection graph (b).

complete dissolution of both Mg^{2+} and Ta^{5+} ions and the phase structural stability may be both ascribed to the improved solubility limit introduced by the high-entropy design. The single-phase structure is preferred in the formation of a highly disordered and multi-component material with high-entropy system.

Figure 2 displays the SEM images of the four samples. Since the samples all exhibit similar sinterability, it can be clearly observed from the graph that the BZMNT component possesses the most desirable dense microstructure with grains closely adjacent to each other. From the grain size distribution plots inserted into their corresponding graphs, the grain size is reduced from ~3 μm on average to submicron size, which can be illustrated by the retardation effect in grain growth

brought by the high-entropy effect. With the increasing designed entropy, the optimum sintering temperature increases for the other three samples, indicating a continuously slowing kinetics in the system [30]. Benefiting from the sluggish diffusion, formation of the crystal structure as well as the crystal fusion, growth, and coarsening are retarded, resulting in a stable structure and reduced grain size of the materials.

Figure 3(a) shows the frequency-dependent dielectric properties of the components which were fabricated at their optimized temperatures. For all samples, both the dielectric constants and loss tangent exhibit frequency independent characteristic in a wide measured frequency range from 1 to 10^5 Hz, which can be considered for use in high-frequency application scenarios. Furthermore, all the components show the similar dielectric behavior of ultra-low loss tangent in the order of 10^{-4}. Figure 3(b) displays the temperature dependence of dielectric constant and loss tangent of BZMNT ceramic measured ranging from 10 Hz to 1 MHz. The dielectric constant has a minor drop over the experimental temperature range from −100 to 200 ℃. Generally, many factors affect dielectric properties (e.g., the grain size effect [31], sintering conditions [32], dopants [33], etc.). In this case, the higher configurational entropy components show a relative higher dielectric constant, i.e., $\varepsilon_{r(BZMN)}$~ 300 > $\varepsilon_{r(BZN)}$~250, and $\varepsilon_{r(BZMNT)}$~220 > $\varepsilon_{r(BZNT)}$~190, at room temperature and 1 kHz. Considering the difference
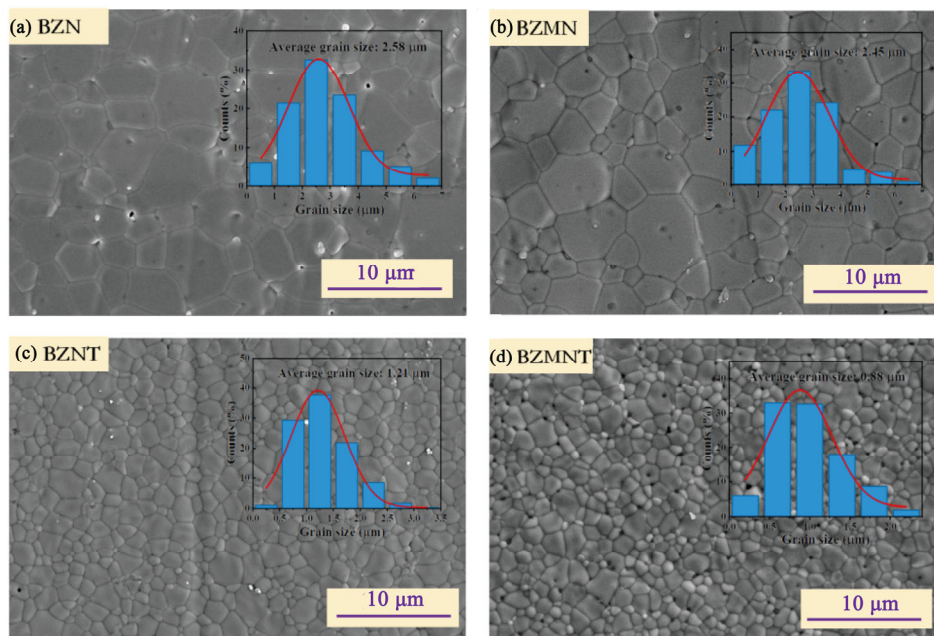
Fig. 2 SEM images of (a) BZN, (b) BZMN, (c) BZNT, and (d) BZMNT (insets are the calculated grain size graphs).
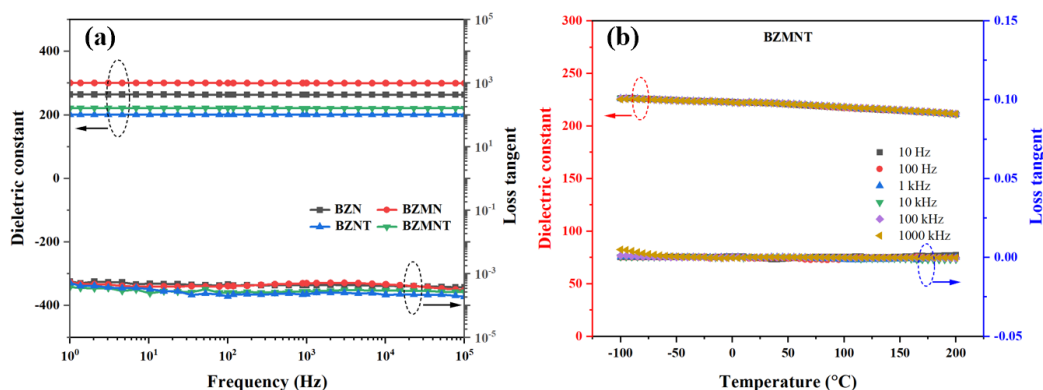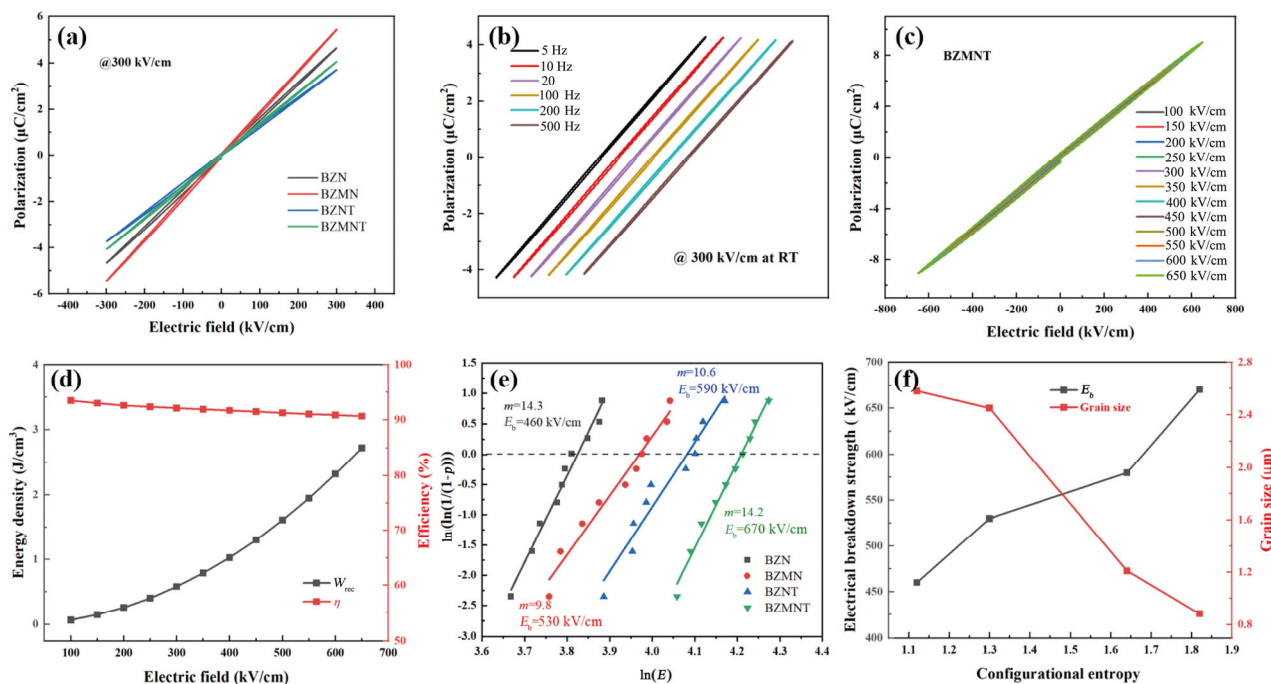
Fig. 3 (a) Frequency dependence measured at room temperature and (b) temperature dependence measured at 10–1000 kHz of dielectric constant as well as loss tangent of BZN, BZMN, BZNT, and BZMNT.

in microstructure, the higher dielectric constant may be related to the lattice distortion caused by the introduction of multi-elements. Besides, the dielectric properties of pyrochlore had a strong correlation with their BO_6-octahedra structure, where B-site ions played the unneglectable roles (e.g., Ta^{5+}) [34]. Moreover, the dielectric temperature coefficient (τ_ε) of BZMNT ceramic is calculated to be ~ -220 ppm/℃ from -100 to 200 ℃, which is much higher than that of pure BZN ceramic ($\tau_\varepsilon = \sim -300$ ppm/℃) over this wide temperature range. The highly structural disorder and lattice distortion brought by high-entropy design may affect the permittivity

temperature coefficient of BZN materials to a more positive value.

The energy storage properties of the high-entropy components are shown in Fig. 4. It can be seen that all the samples possess slim and linear shape *P–E* loops measured at 300 kV/cm and 100 Hz (Fig. 4(a)). Similar ferroelectric behaviors were also proven by other researchers [35,36]. Moreover, the BZMNT ceramic exhibits good frequency stability with negligible polarization and minimal narrowing of the *P–E* loops under different frequencies, as shown in Fig. 4(b). To further illustrate the energy storage behavior of BZMNT

Fig. 4 (a) *P–E* loops measured at 300 kV/cm and 100 Hz of BZN, BZMN, BZNT, and BZMNT; (b) frequency dependence of BZMNT at 300 kV/cm and room temperature; (c) *P–E* loops, and (d) recoverable energy density and efficiency of BZMNT at various applied field; (e) Weibull distribution and the corresponding fitting lines, and (d) calculated E_b and average grain size as a function of configurational entropy of the four samples.
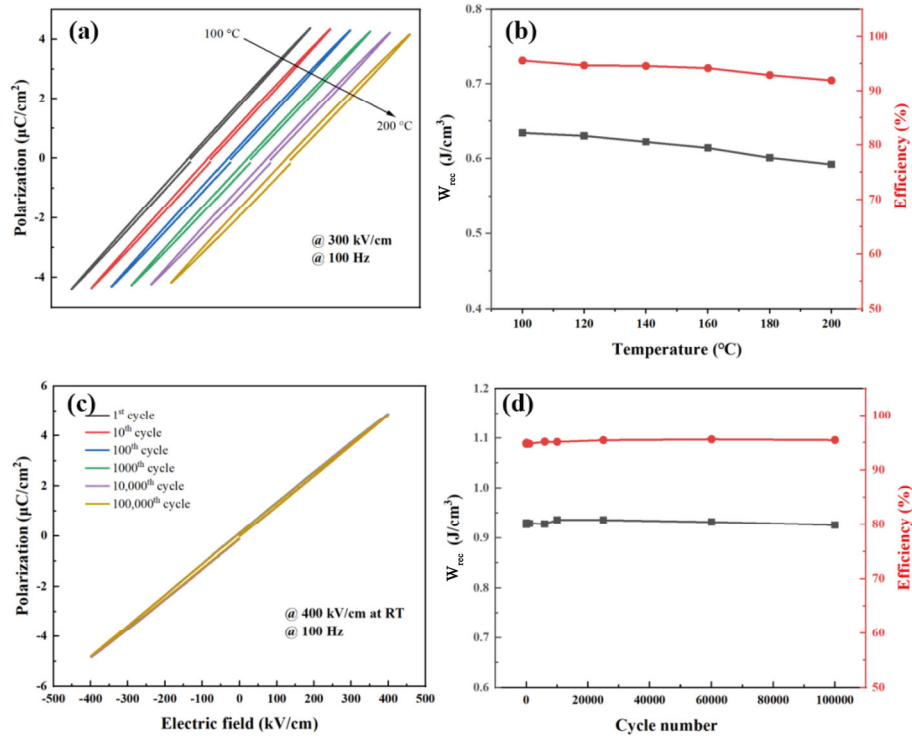
Fig. 5 (a) Temperature-dependent and (c) cycle number dependent *P–E* loops of BZMNT. The W_{rec} and η values of the BZMNT derived from the *P–E* loops as a function of (b) temperature and (d) cycle number.

component, the *P–E* loops at different applied electric fields and 10 Hz are shown in Fig. 4(c), and the summarized energy storage performance is shown in Fig. 4(d). It can be seen that, the BZMNT is able to undergo a continuously elevated applied field without visible deformation of the *P–E* curves. The maximum W_{rec} was obtained at 650 kV/cm of 2.72 J/cm^3 with a high efficiency of 91%. Figure 4(e) displays the Weibull distribution of breakdown strength under direct current (i.e., the E_b of BZN, BZMN, BZNT, and BZMNT are 460, 530, 590, and 670 kV/cm, respectively). Figure 4(f) shows the negative correlation between the BDS and the statistic average grain size of the four samples. The increase in configurational entropy of the materials leads to a smaller average grain size, which is beneficial to the improvement of the BDS in energy storage field.

To evaluate reliability and stability in harsh conditions, fatigue cycling endurance as well as high-temperature stability study were carried out. Figures 5(a) and 5(b) display stable *P–E* loops and the corresponding energy storage performance for BZMNT ceramic under a high temperature range from 100 to 200 ℃. BZMNT exhibits a temperature-insensitive behavior that the efficiency can be still maintained at 92%, and the recoverable energy density has a minor loss of 6.7% at 200 ℃.

Likewise, shapes of the *P–E* hysteresis loop of BZMNT remain the same over the cycling, which can also be perceived from Figs. 5(c) and 5(d). The efficiency maintains 95% without obvious fatigue loss after a cycling number of 10^5, indicating its superior cycling stability (Fig. 5(c)). Whether the cycling or the temperature stability, the excellent performance of the BZMNT ceramic can be attributed to its intrinsically superior properties inherited from base BZN as well as stable structure introduced by high-entropy design, which is beneficial for its application at high temperature and high reliable scenario.

4 Conclusions

In this study, bismuth-based pyrochlore ceramic (BZN) and its three derivates with different configurational entropy were synthesized for the first time utilizing the high-entropy concept. The high-entropy component of BZMNT ($S = 1.82R$) exhibits a moderate dielectric constant (~225) as well as a relatively low loss tangent (~0.0003) at 1 kHz, both of which are beneficial for the enhancement of energy storage properties. The recoverable energy density of 2.72 J/cm^3 and excellent energy efficiency of 91% under an applied electric field of 650

kV/cm are achieved in BZMNT, which is 2 times higher than the origin BZN component. Furthermore, the BZMNT also exhibits superior cycling endurance (no energy density and efficiency loss after 10^5 cycles) as well as temperature- insensitive character (with high energy efficiency of 92% at 200 ℃). All these outcomes demonstrate BZMNT ceramic with high-entropy design a potentially promising dielectric material that can be utilized at high temperatures.

Acknowledgements

References

[1] Pan H, Li F, Liu Y, *et al*. Ultrahigh-energy density lead-free dielectric films via polymorphic nanodomain design. *Science* 2019, **365**: 578–582.

[2] Wang G, Lu ZL, Li Y, *et al*. Electroceramics for high-energy density capacitors: Current status and future perspectives. *Chem Rev* 2021, **121**: 6124–6172.

[3] Yang LT, Kong X, Li F, *et al*. Perovskite lead-free dielectrics for energy storage applications. *Prog Mater Sci* 2019, **102**: 72–108.

[4] Zhang MH, Qi JL, Liu YQ, *et al*. High energy storage capability of perovskite relaxor ferroelectrics via hierarchical optimization. *Rare Met* 2022, **41**: 730–744.

[5] Lin XR, Salari M, Arava LMR, *et al*. High temperature electrical energy storage: Advances, challenges, and frontiers. *Chem Soc Rev* 2016, **45**: 5848–5887.

[6] Zhao PY, Cai ZM, Wu LW, *et al*. Perspectives and challenges for lead-free energy-storage multilayer ceramic capacitors. *J Adv Ceram* 2021, **10**: 1153–1193.

[7] Li DX, Zeng XJ, Li ZP, *et al*. Progress and perspectives in dielectric energy storage ceramics. *J Adv Ceram* 2021, **10**: 675–703.

[8] Zhang RZ, Reece MJ. Review of high entropy ceramics: Design, synthesis, structure and properties. *J Mater Chem A* 2019, **7**: 22148–22162.

[9] Amiri A, Shahbazian-Yassar R. Recent progress of high-entropy materials for energy storage and conversion. *J Mater Chem A* 2021, **9**: 782–823.

[10] Li F, Zhou L, Liu JX, *et al*. High-entropy pyrochlores with low thermal conductivity for thermal barrier coating materials. *J Adv Ceram* 2019, **8**: 576–582.

[11] Cantor B, Chang ITH, Knight P, *et al*. Microstructural development in equiatomic multicomponent alloys. *Mater Sci Eng A* 2004, **375–377**: 213–218.

[12] Yeh JW, Chen SK, Lin SJ, *et al*. Nanostructured high-entropy alloys with multiple principal elements: Novel alloy design concepts and outcomes. *Adv Eng Mater* 2004, **6**: 299–303.

[13] Oses C, Toher C, Curtarolo S. High-entropy ceramics. *Nat Rev Mater* 2020, **5**: 295–309.

[14] Rost CM, Sachet E, Borman T, *et al*. Entropy-stabilized oxides. *Nat Commun* 2015, **6**: 8485.

[15] Rost CM, Rak Z, Brenner DW, *et al*. Local structure of the $Mg_xNi_xCo_xCu_xZn_yO$ (x = 0.2) entropy-stabilized oxide: An EXAFS study. *J Am Ceram Soc* 2017, **100**: 2732–2738.

[16] Chen KP, Pei XT, Tang L, *et al*. A five-component entropy-stabilized fluorite oxide. *J Eur Ceram Soc* 2018, **38**: 4161–4164.

[17] Vayer F, Decorse C, Bérardan D, *et al*. New entropy-stabilized oxide with pyrochlore structure: $Dy_2(Ti_{0.2}Zr_{0.2}Hf_{0.2}Ge_{0.2}Sn_{0.2})_2O_7$. *J Alloys Compd* 2021, **883**: 160773.

[18] Sarkar A, Djenadic R, Wang D, *et al*. Rare earth and transition metal based entropy stabilised perovskite type oxides. *J Eur Ceram Soc* 2018, **38**: 2318–2327.

[19] Dąbrowa J, Stygar M, Mikuła A, *et al*. Synthesis and microstructure of the $(Co,Cr,Fe,Mn,Ni)_3O_4$ high entropy oxide characterized by spinel structure. *Mater Lett* 2018, **216**: 32–36.

[20] Yang WT, Zheng GP. High energy storage density and efficiency in nanostructured $(Bi_{0.2}Na_{0.2}K_{0.2}La_{0.2}Sr_{0.2})TiO_3$ high-entropy ceramics. *J Am Ceram Soc* 2022, **105**: 1083–1094.

[21] Xiang HM, Xing Y, Dai FZ, *et al*. High-entropy ceramics: Present status, challenges, and a look forward. *J Adv Ceram* 2021, **10**: 385–441.

[22] Subramanian MA, Aravamudan G, Subba Rao GV. Oxide pyrochlores—A review. *Prog Solid State Chem* 1983, **15**: 55–143.

[23] Wang XL, Wang H, Yao X. Structures, phase transformations, and dielectric properties of pyrochlores containing bismuth. *J Am Ceram Soc* 2005, **80**: 2745–2748.

[24] Nino JC, Lanagan MT, Randall CA. Phase formation and reactions in the Bi_2O_3–ZnO–Nb_2O_5–Ag pyrochlore system. *J Mater Res* 2001, **16**: 1460–1464.

[25] Da Silva SA, Zanetti SM. Processing of $Bi_{1.5}ZnNb_{1.5}O_7$ ceramics for LTCC applications: Comparison of synthesis and sintering methods. *Ceram Int* 2009, **35**: 2755–2759.

[26] Levin I, Amos TG, Nino JC, *et al*. Structural study of an unusual cubic pyrochlore $Bi_{1.5}Zn_{0.92}Nb_{1.5}O_{6.92}$. *J Solid State Chem* 2002, **168**: 69–75.

[27] Valant M, Davies PK. Crystal chemistry and dielectric properties of chemically substituted $(Bi_{1.5}Zn_{1.0}Nb_{1.5})o_7$ and $Bi_2(Zn_{2/3}Nb_{4/3})O_7$ pyrochlores. *J Am Ceram Soc* 2000, **83**: 147–153.

[28] Tian HY, Wang Y, Wang DY, *et al*. Dielectric properties and abnormal C-V characteristics of $Ba_{0.5}Sr_{0.5}TiO_3$–$Bi_{1.5}ZnNb_{1.5}O_7$ composite thin films grown on MgO (001) substrates by pulsed laser deposition. *Appl Phys Lett* 2006, **89**: 142905.

[29] Sarkar A, Wang QS, Schiele A, *et al*. High-entropy oxides: Fundamental aspects and electrochemical properties. *Adv Mater* 2019, **31**: 1806236.

[30] Ye YF, Wang Q, Lu J, *et al*. High-entropy alloy: Challenges and prospects. *Mater Today* 2016, **19**: 349–362.

[31] Zhao Z, Buscaglia V, Viviani M, *et al*. Grain-size effects on the ferroelectric behavior of dense nanocrystalline $BaTiO_3$ ceramics. *Phys Rev B* 2004, **70**: 024107.

[32] Qi JL, Cao MH, Chen YY, *et al*. Effects of sintering temperature on microstructure and dielectric properties of $Sr_{0.985}Ce_{0.01}TiO_3$ ceramics. *J Alloys Compd* 2018, **762**: 950–956.

[33] Qi JL, Cao MH, Chen YY, *et al*. Cerium doped strontium titanate with stable high permittivity and low dielectric loss. *J Alloys Compd* 2019, **772**: 1105–1112.

[34] Du HL, Yao X. Structural trends and dielectric properties of Bi-based pyrochlores. *J Mater Sci Mater Electron* 2004, **15**: 613–616.

[35] Thayer RL, Randall CA, Trolier-McKinstry S. Medium permittivity bismuth zinc niobate thin film capacitors. *J Appl Phys* 2003, **94**: 1941–1947.

[36] Liu WH, Wang H, Li KC, *et al*. $Bi_{1.5}ZnNb_{1.5}O_7$ cubic pyrochlore ceramics prepared by aqueous solution–gel method. *J Sol Gel Sci Technol* 2009, **52**: 153–157.